metals

MDPI

Article

Revealing the Origin of Heterogeneous Phase Transition and Deformation Behavior in Au-Ag-Cu-Based Multicomponent Alloys

Boning Zhang [1], Li Fu [1], Hualong Ge [1,*], Xuequan Rong [2], Kai Xiong [1], Junjie He [1] and Yong Mao [1,*]

[1] Materials Genome Institute, School of Materials and Energy, Yunnan University, Kunming 650091, China
[2] Key Laboratory of Advanced Materials of Ministry of Education, School of Materials Science and Engineering, Tsinghua University, Beijing 100084, China
* Correspondence: hlge@ynu.edu.cn (H.G.); maoyong@ynu.edu.cn (Y.M.)

Abstract: Local chemical heterogeneity of highly-concentrated multicomponent alloys has drawn much attention as it can produce novel material behaviors and remarkable properties. In Au-Ag-Cu-based multicomponent alloys, phase separation and ordering have long been recognized to correlate with grain boundaries (GBs), but there is still a lack of atomic-scale understanding of the heterogeneous phase transition and how the microstructures respond to deformation. In this paper, a joint experimental and theoretical study was conducted on a medium-entropy polycrystalline model alloy, which is a representative Au-Ag-Cu-based multicomponent alloy with important applications in fields such as photocatalyst and micro-/nano-electromechanical systems. The GB regions are observed to preferentially nucleate two-phase lamellar structures, which are softer than grain interiors featuring short-range-order and modulated morphologies. First-principles calculations suggest the GB segregation of Ag and depletion of Cu are energetically favorable, consequently creating compositions that facilitate phase separation and impede ordering. Calculations of elasticity-based mechanical properties, stacking fault and surface energies reveal the GB lamellar structures are intrinsically soft with heterogeneous deformation capabilities. Furthermore, design strategies based on GB segregation engineering and tuning the dual-phase compositions are proposed to control heterogeneities. The results provide new insights into GB segregation, phase nucleation precursor and mechanical properties of noble-metal multicomponent alloys.

Keywords: multicomponent alloys; grain boundaries; first-principles; phase transition; mechanical properties

Citation: Zhang, B.; Fu, L.; Ge, H.; Rong, X.; Xiong, K.; He, J.; Mao, Y. Revealing the Origin of Heterogeneous Phase Transition and Deformation Behavior in Au-Ag-Cu-Based Multicomponent Alloys. *Metals* **2022**, *12*, 1966. https://doi.org/10.3390/met12111966

Academic Editor: Soran Birosca

Received: 27 October 2022
Accepted: 16 November 2022
Published: 17 November 2022

1. Introduction

Heterogeneity in metallic alloys is a common phenomenon referring to the distinctly nonuniform distribution of specific atoms and varying properties within the medium. As one of the most important sources to develop heterogeneities, the interfaces of crystalline grains—grain boundaries (GBs)—have attracted tremendous research efforts aimed at exploiting these structurally discontinuous regions to improve material properties. Typical examples include applying the GB segregation of boron to design creep-resistant Ni-based superalloys [1], rendering local phase transformations at Mn-enriched GBs to promote toughness in advanced high-strength steels [2], and employing the stabilization effect of segregation to influence sintering process [3] and increase the catalytic activity of nanoparticles [4]. Recently, heterogeneities in multicomponent alloys with high concentrations of several alloying elements, also known as complex concentration alloys (CCAs) or medium/high entropy alloys (HEAs), have attracted special scientific and technical interests, as the complex atomic interactions may generate novel physical phenomena and material behavior. It was found the nano-clustering of principal elements at GBs could

significantly influence the GB cohesion [5], migration of interfaces [6], local phase transitions [7], and the strength-ductility synergy [8]. These clearly demonstrate the significance of GBs with localized structural and chemical characteristics in affecting the mechanical, physical and functional properties of metallic materials [9].

The multicomponent alloys consisting of Group IB noble-metal elements, i.e., Au, Ag, and Cu, have important applications in various fields such as photocatalysts and sensing devices [10], dental implants and jewelry accessories [11], and micro-/nano-electromechanical systems of satellites [12]. In the Au-Ag-Cu ternary system, two types of phase transition, including phase separation and disorder-order transformation, have been widely investigated. In the context of photocatalyst applications requiring unique optical properties, the nanometer-sized thin films of Au-Ag-Cu alloy were used to fabricate diverse types of metallic nanoparticles, such as the solid solution particles precipitating the $L1_0$-Au-Cu ordered phase, and the phase-separated particles showing $L1_2$-Au-Cu_3 ordering with heterogeneous element distribution at GBs [13–15]. For structural applications, several ternary alloys have been assessed regarding the solidus surfaces [16], miscibility gap [17] and ordering reactions [18]. GBs are frequently observed to initiate the phase separation composed of alternating Ag-rich and Cu-rich FCC phases showing a lamellar morphology [19,20]. Moreover, only the Cu-rich phase of the GB lamellar structures was observed to contain ordered nanoprecipitates [21]. When adding a quaternary solute or multiple other elements in Au-Ag-Cu-based multicomponent alloys, the two types of phase transitions were also observed [22]. Similar to that in ternary alloys, the lamellar structures exhibit a general trend to preferentially form at GBs. These suggest the GBs of the Au-Ag-Cu ternary system may play a fundamental role in facilitating the heterogeneous phase nucleation, and it is thus of interest to explore the atomic details of GB chemistry and elucidate how the phase separation interacts with the ordering reactions.

Resulting from the heterogeneous phase transition, the local deformation responses vary in different regions. It was found that isothermal aging causes the GB lamellar structures to have either two-stage hardening responses associated with the phase separation and metastable/stable ordered phases [11] or single-stage hardening associated with the phase separation [21]. Contrary to the age-hardening effect, studies also found that softening occurs at the GB regions with layered Ag-rich phase and nanoprecipitates of ordered phase [23]. The variation of mechanical properties can be explained by thermo-kinetic factors that the aging condition changes the proportions of disordered and ordered phases, and from microstructural factors that the coarsening of lamellar structures decreases the hardening contributions [24]. However, it is extremely difficult for traditional experiments to directly observe the intrinsic deformation characteristics, especially for phases exhibiting varying chemical compositions and degrees of ordering [25,26]. Recent first-principles studies demonstrated that the chemical short-range-order (SRO) significantly affects dislocation mobilities and, consequently, the mechanical properties of refractory [27] and noble-metal [28] HEAs and highly concentrated binary alloys [29]. The theoretical simulations have proven to be invaluable in providing atomic-scale details of the deformation mechanism and elucidating its dependence on elemental/structural heterogeneities.

Designing Au-Ag-Cu-based multicomponent alloys for better material performances requires a comprehensive understanding of the connection between the heterogeneous phase transitions of phase separation and ordering, chemical compositions of phases and the deformation mechanisms. To date, considerable efforts have focused on the phase constituents formed at various processing conditions and the overall mechanical properties. However, the atomic mechanism controlling the heterogeneous phase transitions at GBs and the origin of various deformation responses in phases remain seldom considered. More importantly, there is so far no report on tuning the local phase transformations in a wide chemical composition space to achieve better mechanical properties of Au-Ag-Cu-based multicomponent alloys.

Aimed to unveil the atomistic origin of the phase and deformation heterogeneities in Au-Ag-Cu-based multicomponent alloys, here we conduct a joint experimental and

theoretical study on a medium-entropy ternary polycrystalline alloy. As a representative of Au-Ag-Cu-based multicomponent alloys with complex phase transitions in the grain interior and at GBs, the model alloy also has important applications in various engineering areas. Based on electron microscopy characterizations and first-principles simulations of the model alloy, we propose the heterogeneous phase nucleation and formation of lamellar structures are closely correlated with the GB segregations, where a high driving force for phase separation and the nucleation precursor are provided. In contrast, the heterogeneous element distributions hinder the $L1_2$ ordering process in the GB phases. Notably, the characteristics of both the chemical composition and degree of ordering directly determine the deformation behavior in the grain interior and in the vicinity of GBs. Moreover, the implications of controlling heterogeneities are discussed from perspectives of the segregation engineering of GBs and the composition design of dual-phase structures, respectively. The findings will foster the rational design of noble-metal-based multicomponent alloys for high-performance applications.

2. Materials and Methods

2.1. Material and Microstructure Characterizations

The model alloy containing 28 at.% Au, 20 at.% Ag and 52 at.% Cu was prepared using high-purity (99.999 wt. %) metals by vacuum induction melting, followed by intermediate annealing and cold rolling. The samples with a final diameter of 0.5 mm were solution treated at 750 °C for 1 h and rapidly quenched, and then aged at various temperatures for 10 min in a vacuum. After etching the polished surface in 75% HCl and saturated CrO_3 aqueous solution, the microstructure was observed by scanning electron microscopy (SEM, TESCAN AMBER). The focused ion beam (FIB, TESCAN AMBER) technique was applied to lift out TEM samples, where a 2-step thinning at a voltage of 30 kV and 5 kV, respectively, was performed to obtain sheet samples with a width of ~40 nm, and a final thinning at 2 kV, and a current of 50 pA was used to remove the surface damage induced by Ga ions. The high-resolution transmission electron microscopy (HRTEM, FEI TECNAI F30) characterizations were then conducted on the nanostructures. Micro-hardness tests (SINOWON Vicky MHV-1000) were performed in regions of grain interior and GBs, respectively, with a load of 0.98 N and a holding time of 10 s for more than 6 individual points. Thermodynamics calculations were conducted on the Thermo-Calc 2022a software with the TCNOBL1 database.

2.2. First-Principles Calculations

First-principles calculations can provide valuable predictions and insights into phase equilibrium and mechanical properties. The mcsqs module of Alloy Theoretic Automated Toolkit (ATAT) was used to generate various special quasi-random structures for compositions beyond the dilute limit [30]. To understand the phase transition behavior and the effect of GBs on phase equilibrium in Au-Ag-Cu-based multicomponent alloy, we used the nominal chemical composition of the model alloy to build a category of seventeen SQS supercells with orthogonal axes $[100]$, $[021]$ and $\left[01\overline{2}\right]$. Symmetrical rotation operations around $[100]$ by 53.13° were performed on 1/3 of total atoms, from which fifty-one supercells of Σ5 (021) symmetric tilt grain boundary (STGB) were created to represent general high-angle GBs.

The hardening and deformation mechanisms were investigated through first-principles calculations. The thermo-equilibrium compositions were used to build the $3 \times 3 \times 3$ supercells of FCC-structured Ag-rich, Cu-rich phases and the $L1_2$-structured ordered phase. The elastic constants were calculated based on the stress-strain method, from which the bulk modulus (B), Young's modulus (E), shear modulus (G) and hardness (H_V) were predicted. Besides the elastic properties, we further evaluated the plastic properties of the heterogeneous phase constituents by investigating the unstable stacking fault energies, stable stacking fault energies and surface energies. Using the equilibrium lattice parameters, the 120-atom SQS supercells oriented along $[110]$, $[111]$ and $\left[11\overline{2}\right]$ containing fifteen (111)

layers were chosen. Vacuum layers with a thickness of 13 Å were added to eliminate the interaction between the 2 surfaces. Atom relaxations were allowed along the [111] direction with frozen surface atoms. Up to 36 configurations were used to obtain the distribution of stacking fault energies in each individual phase. The construction of the above models is consistent with that in Refs. [31,32].

First-principles calculations were conducted using the Vienna Ab-initio Simulation Package (VASP) code [33]. The projector augmented wave (PAW) method [34,35] with the valence electron configurations Au: $5d^{10}6s^1$, Ag: $4d^{10}5s^1$, and Cu: $3d^{10}p^1$ was adopted. The generalized gradient approximation (GGA) [36] and PBEsol exchange-correlation function were used to accurately describe the structural and enthalpy-related properties [37–39]. After converging tests of total energy and lattice parameter, a plane wave cut-off energy of 500 eV, a first-order Methfessel-Paxton method [40] with the smearing of 0.1 eV, and the Monkhorst-Pack k-mesh [41] with a spacing of 0.02 $Å^{-1}$ were chosen in all calculations. The relaxation criterion was set at 10^{-6} eV and 10^{-2} eV $Å^{-1}$, respectively, for electronic and ionic relaxations. These parameters will ensure sufficient high accuracies of energetics and atomic forces.

3. Results

3.1. Nanostructure Characterizations in the Grain Interior and at GBs

Phase separations combined with disorder-order phase transitions are critical for the mechanical properties of Au-Ag-Cu-based multicomponent alloys. We first conducted thermo-equilibrium calculations on Thermo-Calc before experimental investigations. The results suggest that the model alloy passes through a miscibility gap at 731 °C with phase separation into Cu-rich and Ag-rich FCC phases. With decreasing temperature to 370 °C, the formation of the L12-type ($AuCu_3$) ordered phase occurs. Based on the results, the cold-rolled Au-Ag-Cu alloy was solution treated at 750 °C before aging at 350 °C and 450 °C for 10 min, respectively. The two representative aging conditions are considered to satisfy the need to induce heterogeneous phase transition and enable a comparison of local deformation responses.

Figure 1 shows the TEM morphologies of the aged matrix grains and corresponding diffraction patterns. Clearly, the bright-field images show microstructure modulation manifested as cross-hatched patterns, indicating spinodal decomposition during the isothermal holding [42]. We confirmed from the indexed diffraction patterns that the modulation occurs along the [001] direction in the two samples [21]. Compared with that of the low-temperature aging at 350 °C, the width and length of the bright bands are coarser, in the range of 5~10 nm, for the 450 °C aged matrix. Furthermore, weak super-lattice reflections caused by the L12-type $AuCu_3$ ordered phases are visible inside the patterns. The ordered nanoprecipitates are crystallographic parallel to the matrix along basic orthogonal axes of $[100]_{FCC} \parallel [100]_{L1_2}$, $[010]_{FCC} \parallel [010]_{L1_2}$, $[001]_{FCC} \parallel [001]_{L1_2}$ with the cube-on-cube orientation relationship, which was similarly reported in Au-Ag-Cu metallic nanoparticles [15].

The formation of lamellar structures after aging was observed by electron microscopy techniques. Figure 2a,b shows the SEM image for the typical distribution of lamellar structures in the aged specimens, where the lamellar structures are primarily distributed at GBs and GB triple junctions. A comparison between different aging conditions shows that the volume fractions of lamellar structures are higher in the high-temperature aged samples. The FIB technique was used to lift out lamellar samples from the position closest to GBs for further TEM observations. As shown in Figure 2c, the lamellar structures are composed of alternating layers in width of several tens of nanometers, which were confirmed by energy dispersive spectroscopy (EDS) analysis to be Cu-rich and Ag-rich phases, respectively. The indexed diffraction patterns suggest the two FCC structures have $[310]_{Ag\text{-}rich} \parallel [111]_{Cu\text{-}rich}$ parallel directions, in contrast to the cube-on-cube orientation relationship resulting from spinodal decompositions. Moreover, there were neither side bands nor characteristic satellites observed in the diffraction patterns, suggesting the lamellar structures are precipitated by a nucleation and growth mechanism rather than spinodal decomposition. The HRTEM

characterization and fast Fourier transformation (FFT) in Figure 2d indicate that the ordered nanoprecipitates could co-exist in the two separated phases, while the developed degrees of chemical SRO are qualitatively lower than that of the grain interior. Earlier studies proposed the formation of GB lamellar structure is correlated with the migrating GBs through a discontinuous precipitation mechanism, where the growth of lamellar structures starts from GBs and proceeds by migrating GBs with a cellular shape at the expense of coarse modulate matrix containing ordered nanoprecipitates [21]. Considering the fact that the initial phase nucleation state does not necessarily require the migration of interfaces, the above observations imply that the heterogeneous phase transition near GBs involves the competition between phase separation into lamellar structures and the chemical ordering process, thereby affecting the consequent phase constituents and local deformation behaviors.

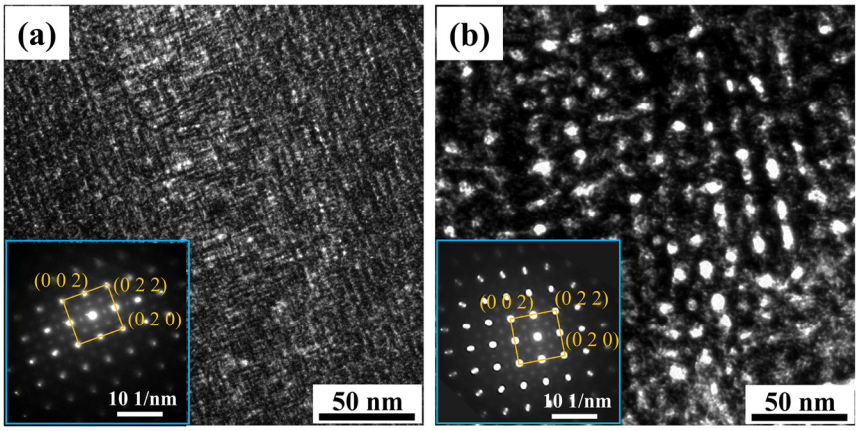

Figure 1. The TEM images and diffraction patterns in the matrix after aging at (**a**) 350 °C and (**b**) 450 °C.

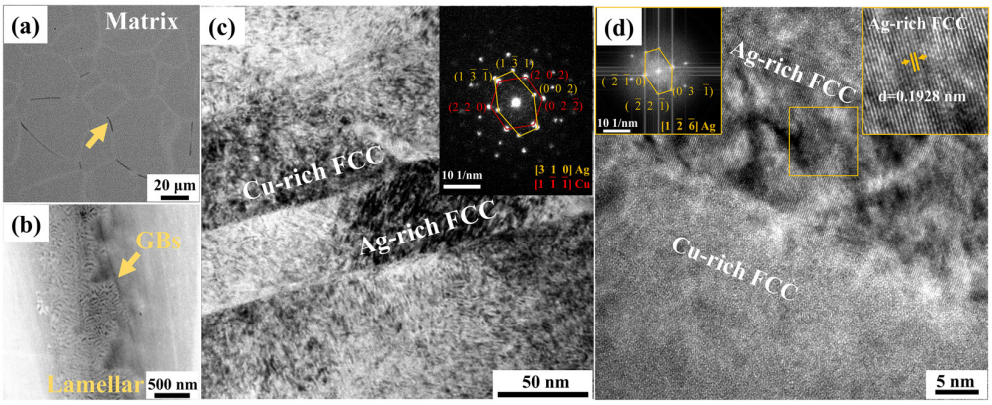

Figure 2. Experimental characterization of the GB phases in samples after solution treatment and isothermal aging at 350 °C. (**a**) The SEM image of the microstructure. (**b**) The locally enlarged SEM image of the lamellar structure near GBs; (**c**) The TEM bright field image of the lamellar regions with corresponding diffraction patterns showing FCC structures of Ag-rich and Cu-rich phases; (**d**) The HRTEM micrograph of GB phases with corresponding diffraction patterns obtained by FFT.

3.2. The Local Deformation Behavior of the Heterogeneous Microstructures

To evaluate the mechanical responses in the heterogeneous microstructure, the Vickers hardness tests were performed on the isothermal-aged samples. Figure 3a compares the local hardness between the grain interior and the GB lamellar structures. Both the matrix and GB lamellar regions show hardening effects after a short time aging of 10 min. Compared with the grain interior, the GB lamellar structures have significantly lower values of hardness. Aging at a higher temperature of 500 °C also causes an increase in local

hardness, while the magnitude of the increase is limited. Figure 3b shows that while a small area of the indentation may be outside of the GB lamellar region, aging indeed caused hardening effects in the multicomponent solution-treated samples, which has a hardness value as represented by the dashed line. At the stress-concentrated regions around the corner of indentations, preferential propagations of micro-cracks in the lamellar structures are visible, in contrast to that in the grain interior. The above observations indicate that the phase constituents possess different hardening mechanisms and plastic properties.

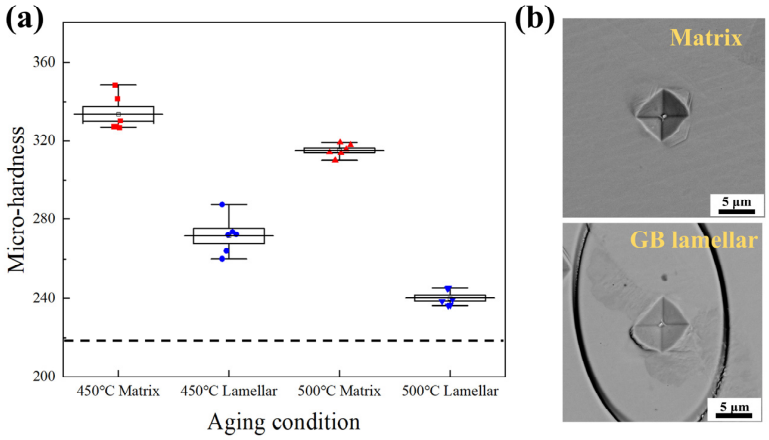

Figure 3. The Vickers hardness test. (**a**) The hardness values in grain interior and lamellar structures near GBs after aging for 10 min, as compared with that of solution-treated specimens (dash line); (**b**) Illustrations of the indentations in matrix and GB lamellar regions. The FIB technique was used to mark the lamellar regions before the tests.

Besides the interfacial characteristics of the GB lamellar structures, the inherent deformation behavior of Ag-rich and Cu-rich phases are also crucial to mechanical responses. To explore the deformation details and microstructure factors determining the mechanical response of the GB lamellar structures, we then lifted out TEM samples from the area close to the indentation. As shown in Figure 4, the heterogeneous distributions of alloying elements are superimposed on the high-angle annular dark field (HAADF) image. The white arrows in Figure 4 indicate that straight and wavy dislocation lines can be observed along the longitude direction of lamellar structures. Interestingly, the dislocations were primarily found in the Cu-rich phase but not in the Ag-rich phase. This suggests the inherent differences in the deformation mechanisms of the separate phases during deformation. In addition, as the dislocation density in the Cu-rich phase is high, it also implies that the low fraction of ordered nanoprecipitates in the Cu-rich phase plays a minor role in affecting the deformation.

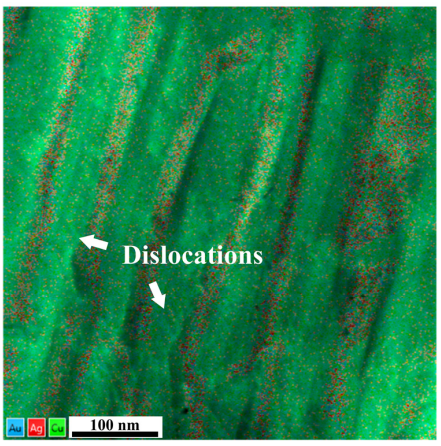

Figure 4. The TEM observation of dislocations in the GB lamellar regions near the indentation.

3.3. First-Principles Calculation of Phase-Transition Characteristics

A category of seventeen SQS supercells using the nominal composition of the investigated Au-Ag-Cu model alloy was generated, from which a total number of fifty-one GB supercells was used for DFT calculations. Figure 5 illustrates one example that the symmetrical rotation operation was performed on the part of the bulk supercell to generate the Σ5 (021) STGB supercell. Accounting that phase separation accompanying $L1_2$ ordering in the ternary system is closely associated with the nearest-neighbor atoms, the SRO parameter of different chemical bonding pairs [5], i.e., Au-Au, Au-Cu, Au-Ag, Cu-Cu, Cu-Ag, and Ag-Ag, were evaluated. Further analysis indicates the structures are adequate to describe the phase transition characteristics through quantification of the various bonding pairs.

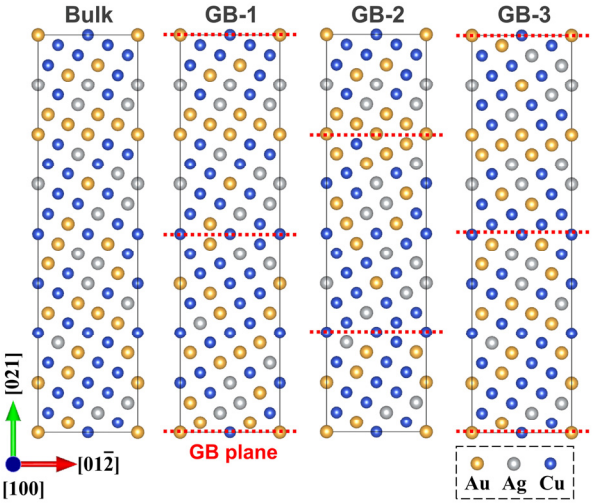

Figure 5. Schematic of one disordered bulk supercell and three GB supercells obtained by rotation.

The SRO parameters of the bulk supercells are shown as a radar plot in Figure 6a. Different magnitudes of phase separation (positive SRO) and ordering (negative SRO) can be obtained. Figure 6b shows the Pearson correlation coefficient between the total energy of the relaxed bulk supercell and the number of different bonding pairs, where a negative (positive) value suggests the bonding pairs are energetically favorable (unfavorable) to stabilize the system. We found a strong tendency to form SRO between Au and nearest-neighbor Cu atoms, whereas the Au-Au, Au-Ag and Cu-Cu pairs are less likely to form due to the increase in total energies. High confidence in the results can be expected from the relatively low statistical significance values ($p < 0.05$). It suggests that the $L1_2$-Cu_3Au ordered phase is unambiguously preferential to precipitate in the quenched alloy matrix at 0 K, whereas the phase separation of Ag-rich and Cu-rich phases is less likely. The first-principles data conform to that of experimental characterizations in previous sections. Figure 6c shows the statistics of the bonding length up to the third-nearest neighbor, which further suggests there exists local structural disorder or lattice distortion in the medium-entropy Au-Ag-Cu system. This observation is similar to that reported in other multicomponent alloys [43,44]. Especially, the nearest-neighbor Cu-Cu bonds tend to have the smallest average distance.

As seen in Figure 6d for the relaxed GBs, a Gaussian-type distribution of GB energies with an average value of 0.59 J/m^2 and a standard error of 0.14 J/m^2 can be found. The mean value of GB energy is comparable to that of pure Au [45]. To determine the effect of local chemistry on the GB energies, the adaptive common neighbor analysis (CNA) method was applied to identify GB atoms in the GB supercells without atom relaxation. The Pearson correlation between GB energy and the number of various bonding pairs within the GB region is plotted in Figure 6e. As seen from the magnitudes of P values, the numbers of Cu-Ag and Ag-Ag bonds are significant to exhibit strong negative correlations with the GB energy, suggesting that the formation of these bonds lowers the GB chemical

energy. After relaxation, we found the trend still holds, although the significance may be reduced to some extent. This suggests that both chemical and structural effects influence GB energy, and it will be discussed in the following results of GB segregation. In contrast to the bulk region favorable of Au-Cu bonds which are related to the $L1_2$ ordering, the GB region is found to show a different tendency of phase transition, with a high number of Ag-Ag bonds as a manifestation of promoting the phase separation. The distribution of bonding length within the GB region was also calculated, as shown in Figure 6f. Among the various bonding pairs, the nearest-neighbor Cu-Cu bonds again show the smallest average length, which is the same as the case in the bulk region. However, much larger lattice distortions were found for GB atoms, manifested as the smaller Cu-Cu and larger Ag-Ag interatomic distances than that in the bulk, respectively. With the strong interfacial disordering at GBs, co-segregation of Ag and Cu is expected to be further prompted.

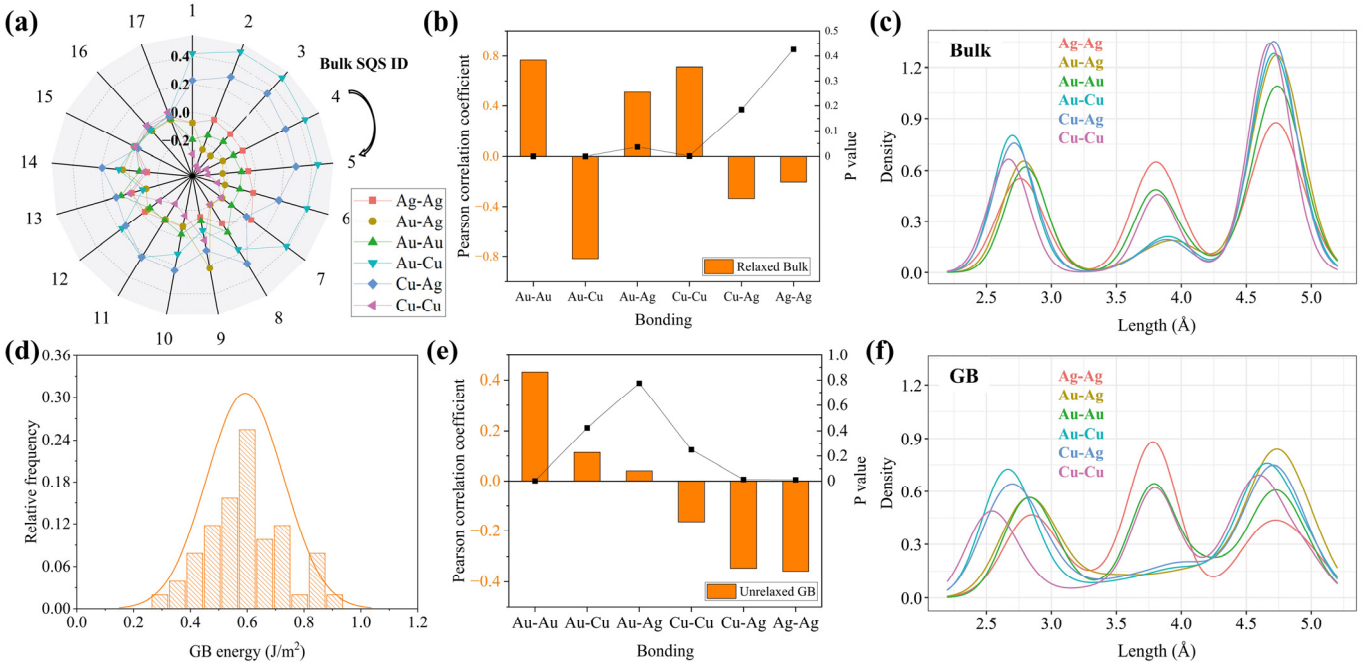

Figure 6. The DFT calculation of the phase-transition characteristics. (**a**) The chemical SRO in the bulk supercells. (**b**) The correlation between the number of bonds and total energies of the relaxed bulk supercells. (**c**) The bond length distributions in the relaxed bulk supercells. (**d**) The distribution of GB energies. (**e**) The correlation between the number of bonds in the GB region and the GB energy before structural relaxations. (**f**) The bond length distributions in the GB regions.

The above calculations of GB energetics and bonding characteristics strongly indicate the prevailing role of high-angle GBs in affecting phase separation and ordering. We, therefore, analyzed the chemical and structural effects of GBs on equilibrium segregation to further understand the heterogeneous phase transitions. The correlations between the distribution of atoms and the GB energy without atomic relaxation, as well as the energy reduction during relaxation ($\Delta\gamma$), were evaluated. As shown in Figure 7, the DFT calculations predict that the GB segregations of Cu and Ag decrease the unrelaxed GB energy while Au increases the energy. The coefficient of Ag is more negative than that of Cu, which implies the GB segregation of Ag should be more important to influence the local phase transitions. Contrarily, we observe opposite trends for the correlation coefficients between GB chemistry and $\Delta\gamma$. For instance, as more Ag atoms segregate to the GB, the induced structural contributions to reduce the GB energy become smaller. This suggests that the chemical effect on GB energies can be compensated by the structural effect. It should be noted we found the P values are smaller than 0.05 in all cases, which supports

the test hypothesis that the GB chemistry in the ternary system does play a role in affecting the GB energy.

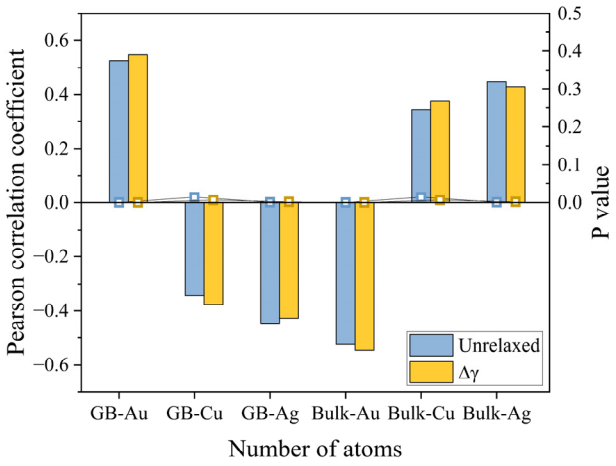

Figure 7. The correlation between the number of different atoms in different regions and the unrelaxed GB energy and the energy decrease during relaxation ($\Delta\gamma$).

3.4. Atomic-Scale Calculation of Mechanical Property and Deformation Mechanisms

First-principles calculations were performed to predict the elastic and plastic properties of the individual phase-transition product and to gain insights into the atomic-scale deformation mechanisms. The compositions of the equilibrium phases at 450 °C obtained from Thermo-Calc calculations were used to generate the SQS supercells. Accounting that the $L1_2$ phase maintains almost the same composition as the disordered Cu-rich phase, we then constructed the highly ordered $L1_2$ supercells where the Ag atoms are distributed randomly at all lattice sites, while Au and Cu atoms occupy the corner and face-centered sites, respectively.

The calculated lattice parameters are summarized in Table 1. As compared with the disordered FCC matrix with the nominal composition of the model alloy, the decomposed Ag-rich (Cu-rich) phase shows a larger (smaller) lattice parameter, which agrees well with HRTEM characterizations in Figure 2c. Although the interface misfit between the two phases is small (<0.02), interfacial dislocations are expected to release the coherency strains and contribute to hardening. All the phases were confirmed to be mechanically stable at 0 K according to Born–Huang's criteria of lattice stability [46]. The elastic constants (C11, C12, C44) were used to approximate the bulk modulus (B), Yong's modulus (E) and shear modulus (G) of polycrystals. We see the ordered structure has the largest values of elastic parameters among the multicomponent solid solutions, followed by the Cu-rich and Ag-rich disordered phases. The intrinsic hardness (H_V) values, as predicted by Chen's model [47] in Table 1, show the decomposed phases are inherently softer than the ordered phase. This demonstrates that the higher micro-hardness of the matrix than GB lamellar structures in previous experimental tests stems from the ordered phase. Besides, the H_V/E parameter, which is an effective indicator of tribological behaviors and has a negative correlation with the wear rate [48,49], suggests a better service performance for local regions precipitating the ordered phase.

The plastic deformation mechanisms of phases were then evaluated by calculating the unstable stacking fault energies γ^{USF} and stable stacking fault energies γ^{SFE}. As shown in Figure 8a, the average stacking fault energies of the Ag-rich phase are lower than that of the Cu-rich phase. However, larger variations of γ^{USF} and γ^{SFE} were found in the Cu-rich and Cu-order phases. With the transition from disordered to ordered structure, the average γ^{USF} and γ^{SFE} are increased, indicating increased activity of dislocations. Interestingly, the γ^{SFE} in the Cu-rich disordered phase could even become negative for certain faulting planes, which implies the Shockley partials will become predominant over

perfect dislocations during deformation [50]. Besides, the original FCC will be locally metastable and can transform into a nanoscale HCP phase [51]. Using the same supercells, the (111) surface energies of phases are plotted in Figure 8b, which shows the Ag-rich disordered phase has the lowest surface energies.

Table 1. First-principles calculation of the lattice parameters (a, Å), elastic constants matrix (C11, C12 and C44, GPa), bulk modulus (B, GPa), Young's modulus (E, GPa), shear modulus (G, GPa), hardness ($H_{V\text{-}Chen}$, GPa) and the effective indicator of wear-resistance (H_V/E) for various phases.

Phases	a (Å)	C11 (GPa)	C12 (GPa)	C44 (GPa)	B (GPa)	E (GPa)	G (GPa)	$H_{V\text{-}Chen}$ (GPa)	H_V/E
Nominal FCC	3.8655	187.7	139.9	61.0	155.8	115.1	41.8	0.8	0.007
Ag-rich	4.0393	165.5	119.1	56.7	134.5	108.2	39.6	1.1	0.010
Cu-rich	3.7825	200.1	148.9	69.6	165.9	127.7	46.5	1.3	0.010
AuCu-order	3.7312	211.4	148.2	79.6	169.3	148.7	54.9	2.6	0.017

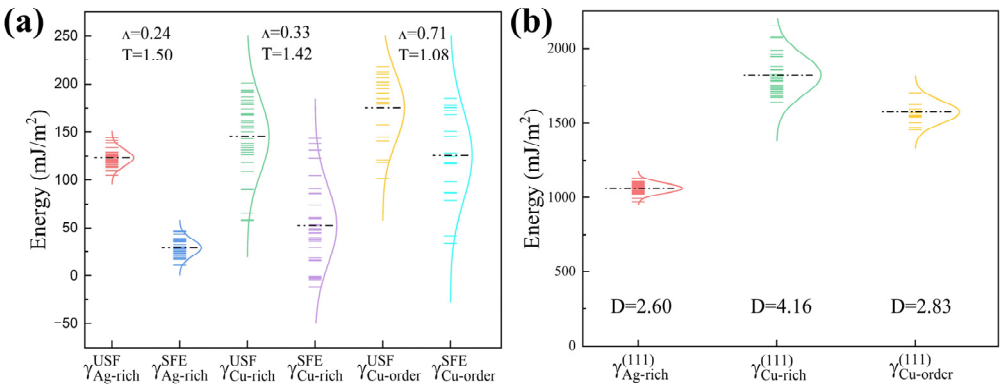

Figure 8. Prediction of plasticity and deformation mechanisms in the different phases. (**a**) The unstable (γ^{USF}) and stable (γ^{SFE}) stacking fault energies with the characteristic ratio Λ and the twinnability measure T. (**b**) The surface energies with the ductility parameter D.

According to the universal scaling of planar fault energy barriers in FCC metals [52], the material characteristic ratio

$$\Lambda = \gamma^{SFE}/\gamma^{USF}, \tag{1}$$

and the twinnability measure

$$T = \sqrt{(3 - 2\Lambda)/\left(1 + \frac{\Lambda}{2}\right)}, \tag{2}$$

can reveal the relative importance of partial or full dislocation emission vs. micro-twin emission from crack tips under deformation. Among the three phases, it is predicted the Ag-rich phase with the smallest Λ and the largest T value is more favorable for twin emission. When a high degree of SRO is developed in the Cu-rich phase to form the $L1_2$ phase, the twinnability is decreased, i.e., emission of trailing partial dislocations becomes favored over twins. The above calculations are qualitatively consistent with experimental observations in Figure 4, where more dislocations are initiated in the Cu-rich phase of GB lamellar structures. Moreover, the ductility parameter

$$D = 0.3\frac{\gamma^{Surf}}{\gamma^{USF}}, \tag{3}$$

which indicates the susceptibility to cracking according to the Rice-criterion [53], were calculated using the average surface energies and unstable stacking fault energies of the three phases. The $D > 1$ values suggest the energy barrier of cleavage is higher than that of

the dislocation nucleation [54]. While all the phases are generally ductile, the Ag-rich FCC phase is relatively brittle and more likely to initiate and propagate cracks. This explains the frequently observed micro-cracks near indentations at the GB lamellar regions with coarsened layers of the Ag-rich phase.

4. Discussion

4.1. The Effect of GB Segregation on Phase Separation and Ordering

The phase stability is of particular interest in studies of multicomponent alloys. Even with a high configurational entropy to stabilize the solid solution, phase transition takes place due to the strong interactions between atomic pairs. Especially, GBs, as the most ubiquitous defects of polycrystalline materials, are preferential to nucleate phases [55–57]. For instance, the Fe-35Ni-35Mn (at%) medium-entropy alloy show $L1_0$-NiMn ordering and phase separation, while the latter can primarily occur at GBs with localized Mn clustering [58]. In the current Au-Ag-Cu model alloy, the modulated morphology and the superlattice spots (Figure 1) indicate that spinodal-type phase separation accompanies the $L1_2$ chemical ordering process in the grain interior. However, the phase separation exhibiting lamellar morphologies and containing a low fraction of ordered nanoprecipitates can be directly observed in the vicinity of GBs. Previous experiments indicated that the formation of GB lamellar structures in noble-metal multicomponent alloys might be stimulated by the decrease of lattice strains [24]. A similar observation was also explained by the attractive interactions between particular elements [59].

Through first-principles modeling of the bulk and GBs in the multicomponent Au-Ag-Cu alloy, we found the critical role of interfacial chemistries in affecting the local phase constituents. The calculations reveal that Ag and Cu atoms are energetically favorable to enrich at the high-angle GBs, while the Au concentration is depleted. This is consistent with recent experimental observations of Au-Ag-Cu metallic nanoparticles where the incoherent GBs are primarily segregated by Ag [13]. The GB segregation is therefore expected to provide a high chemical driving force for the Ag-Cu phase separation [60]. Contrarily, the ordering process is hindered due to decreased concentrations of Au (Figure 6). To validate the first-principles predictions that GB segregation is the precursor state to nucleation and heterogeneous phase transformations, thermodynamics calculations were further conducted using different Au concentrations. Figure 9 demonstrates the miscibility gap expands to the liquidus temperature with decreasing Au content, thus facilitating the formation of the eutectic-like lamellar structures. However, the ordering occurs from $L1_0$ to $L1_2$, showing a decreasing Au/Cu ratio from 1 to 1/3, and the $L1_2$ phase region shrinkages until it completely disappears. It is evident from the pseudo-binary phase diagrams that local chemical composition affects both the phase separation of the Ag-Cu system and the ordering of the Cu-Au system. The results evidenced that the difference of phase constituents in grain interior and at GBs originates from the local solute supersaturations at GBs, which would provide a comprehensive understanding of the phase transition precursors and nucleation mechanisms in multicomponent alloys.

The above results point to a feasible design strategy to modulate heterogeneous phase transitions through GB engineering of solute segregations. Firstly, we propose tuning the thermodynamic driving force for GB segregation via multiple solute interactions is of crucial importance to hinder the heterogeneous phase transition in multicomponent alloys. By using the segregation and mixing enthalpies from binary subsystems, a lattice-type model for describing GB segregation in ternary alloys [61] was extended to quinary non-equimolar HEAs, which yields qualitatively consistent results with atomistic simulations [62]. The model could provide useful guidance for the design objective to prevent the phase separation products from exhibiting poor mechanical properties. For example, we may add a quaternary solute X in the Au-Ag-Cu ternary system to produce competitive GB segregations with Ag according to thermodynamic parameters as tabulated in Ref. [63]. The candidate solutes should ideally have negative values of $\Delta H^{seg}_{Au,\,X}$, $\Delta H^{seg}_{Ag,\,X}$, $\Delta H^{seg}_{Cu,\,X}$ and negative values of $\Delta H^{mix}_{Au,\,X}$, $\Delta H^{mix}_{Ag,\,X}$, $\Delta H^{mix}_{Cu,\,X}$ to enhance the GB segregation of X, while

negative value of $\Delta H^{seg}_{X,Ag}$, $\Delta H^{mix}_{X,Au}$ $\Delta H^{mix}_{X,Cu}$ and a positive value of $\Delta H^{mix}_{X,Ag}$ to decrease the GB segregation of Ag, where the negative $\Delta H^{seg}_{A,B}$ represents that solute B tends to segregate to GBs in solvent A. Further studies are encouraged to realize a quantitatively accurate prediction of GB segregations and thus heterogeneous phase transition in Au-Ag-Cu multicomponent alloys [64]. Secondly, as the lamellar morphologies at GBs are correlated with migrating interfaces, the diffusion kinetics of atoms and migration of GBs play a role in the initiation of heterogeneous phase transitions. Previous studies suggest that the GB segregation of Nb atoms in the $(CoCrFeNi)_{94-x}Al_3Ti_3Nb_x$ (at.%) HEA can inhibit GB diffusion of alloying atoms and retard GB migration, consequently hindering the heterogeneous phase transition at GBs [65]. It indicates exploiting the solute drag effects that retard GB migrations [66] as a kinetic controlling factor helps to regulate the formation of heterogeneous phase transitions. Moreover, we note the preferential phase separation near GBs can be initiated not only by the equilibrium segregation during isothermal holding but also by the inter-dendrite segregation after solidification. Controlling the non-equilibrium solidification is also a possible route. Hence, both thermodynamic and kinetic factors should be considered to minimize the discontinuous phase separation at GBs.

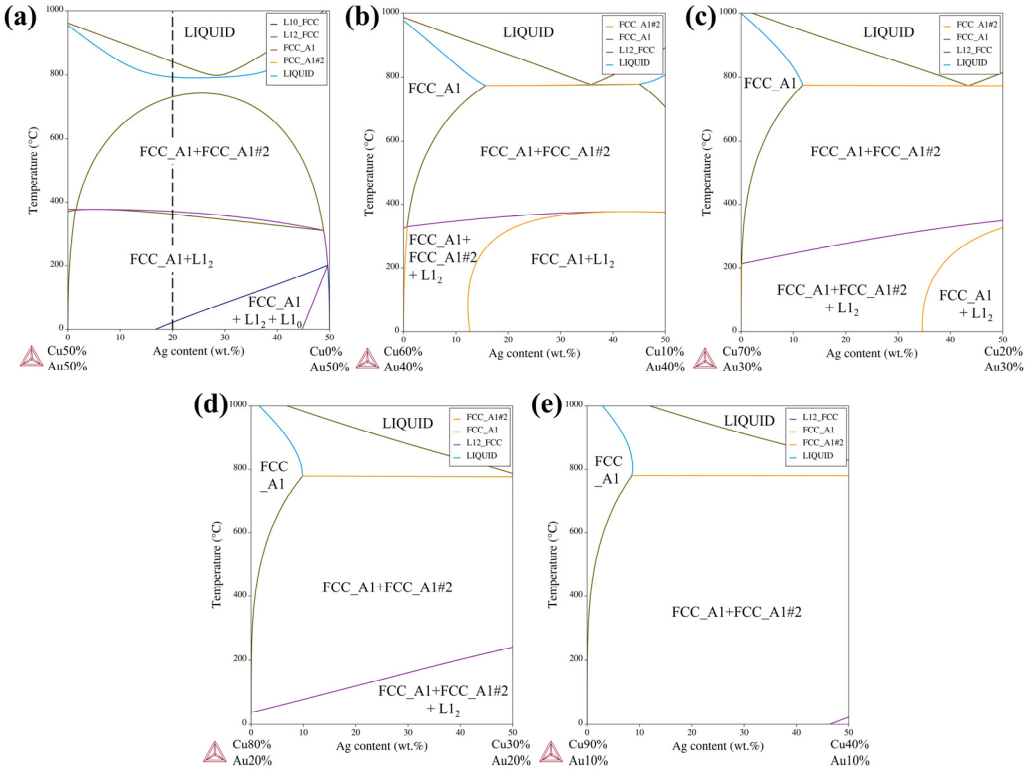

Figure 9. The Ag-Cu pseudo-binary phase diagrams. (**a**) 50 wt. % Au; (**b**) 40 wt. % Au; (**c**) 30 wt. % Au; (**d**) 20 wt. % Au; (**e**) 10 wt. % Au.

4.2. Strengthening in Different Phases and Implications for Alloy Design

Age hardening is critical to obtain a high service performance of Au-Ag-Cu-based multicomponent alloys. Previous studies have shown that ordering in the matrix dominates the hardening, while the GB precipitates composed of ordered phase, and stable Ag-rich phase could decrease the local hardness [23]. However, the hardness decrease was attributed to the microstructural coarsening of the lamellar structures rather than the types of metastable or stable product phases [24]. The model alloy, as a representative of the Au-Ag-Cu multicomponent, was used in this study to explicate the solid solution strengthening and deformation mechanisms in different phases.

From microhardness tests, we found strong age-hardening effects in the grain interior, while the lamellar structures near GBs show relatively lower hardness values (Figure 3). By ab-initio prediction of the intrinsic hardness, solid solution strengthening was validated in the disordered FCC phases with a higher Ag or Cu content than the nominal composition. We see significant hardening occurs when a high degree of chemical SRO is developed in the Cu-rich phase (Table 1). The calculations demonstrate that the ordering process in the Cu-rich phase dominates the strengthening increment. Accounting that the Ag-rich and Cu-rich phases grow cellularly as alternating layers in the lamellar structures, the low-hardness Ag-rich phase causes a large indentation area due to its coarsened width up to several tens of nanometers. We emphasize the deformation mechanisms are different in the heterogeneous phase transition products. More dislocations were observed in the Cu-rich phases (Figure 4), which seems to contradict its relatively high hardness. First-principles simulations revealed that the disordered Cu-rich phase features a higher average γ^{USF} than the Ag-rich phase, with even negative γ^{SFE} on certain planes (0). This means that compared with the Ag-rich phase, the emission of partial or full dislocations is favored in the Cu-rich phase, which agrees well with the characterizations of dislocations in the deformed nanostructure. When the degree of local chemical SRO is enhanced, the stacking fault energies are also increased. Thus, the deformation is predicted to be correlated with the chemical SRO [67], which can be understood as the result of some stable atomic pairs increasing defect energies. The strong correlation between SRO and deformation was also reported in CrCoNi medium-entropy alloys with local chemical order around Cr atoms [68].

The above findings suggest the deteriorating effect of the lamellar phases at GBs originates mainly from the Ag-rich phase, which exhibits a low hardness and ductility. To guide the design of Au-Ag-Cu alloys with a highly uniform microstructure and local deformation responses, here we explore the correlation between phase composition and yield strength through the mechanistic model that assumes individual atoms interact with dislocations in an average FCC alloy matrix [28,69]. Figure 10a shows at a temperature of 300 K, and a strain rate of 10^{-4} s^{-1}, more than 5000 chemical compositions in the full composition space of the Au-Ag-Cu ternary system were evaluated and numbered according to an increasing sequence of the predicted strength. Then every 100 compositions were averaged to illustrate the general correlation between phase chemistry and strength, where we see a higher Cu concentration of the disordered FCC phase generally features a higher yield strength, in contrast to the effects of Au and Ag. Integrating the model with thermodynamics calculations in the full composition space and the rule-of-mixtures inputs, the dependence of yield strength on alloy composition, phase fraction, and the experimental testing conditions can be predicted. For instance, the strength difference in the two-phase region after aging at 450 °C is plotted in Figure 10b. Obviously, the difference is large in the middle region with Au concentrations in the range of 48~55 wt. %. This explains the large difference in local hardness observed in the current model alloy with 50 wt. Au%. The average yield strength was then calculated by considering the phase fraction in the ternary system. As suggested in Figure 10c that the highest strength is not located at the Cu-rich corner; the overall mechanical properties in heterogeneous microstructures are determined by the characteristics of phase constituents rather than the alloy composition. The results will provide helpful directions for composition design to achieve high strength and homogeneities of local mechanical properties in Au-Ag-Cu-based multicomponent alloys.

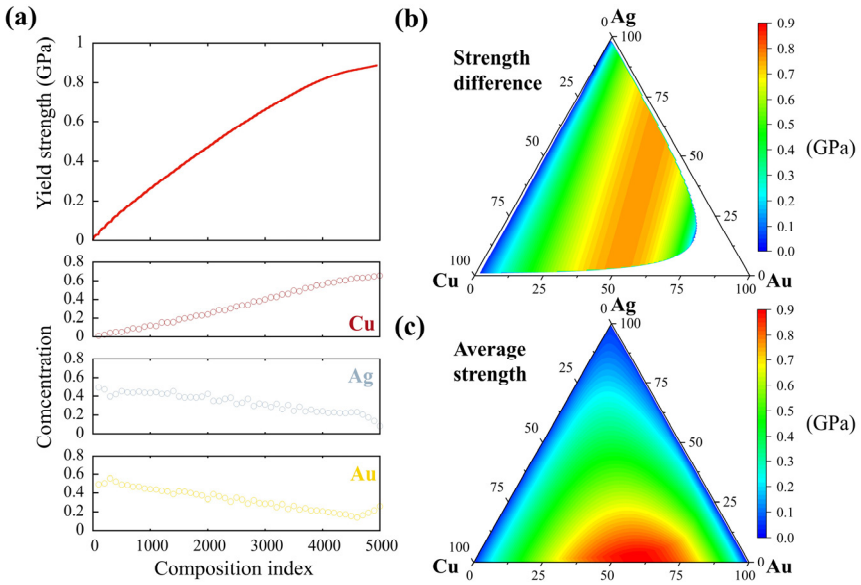

Figure 10. The first-principles-based prediction of yield strength in the full composition space. (**a**) The dependence of yield strength on alloying concentration in disordered FCC phase. (**b**) The strength difference between the Ag-rich and Cu-rich phases in the two-phase region. (**c**) The average yield strength in the ternary Au-Ag-Cu alloy according to the rule of mixtures. The compositions are in wt. %.

5. Conclusions

To summarize, the atomic-scale origin of heterogeneous phase transition and deformation behaviors in a medium entropy Au-Ag-Cu model alloy was investigated through a combination of experimental characterizations and first-principles calculations. We reveal the close correlation between GB segregation, different phase constituents and the local deformation responses in Au-Ag-Cu-based multicomponent alloys. The high-angle GBs are found to be favorable for the segregation of Ag and depletion of Au, which then could create localized composition regions rendering phase separation and formation of lamellar structures. Contrarily, the $L1_2$ ordering is less likely to take place. The Ag-rich phase is suggested to be intrinsically soft and susceptible to cracking, and the two separated disordered phases lacking chemical ordering in the GB lamellar structures exhibit heterogeneous deformation capabilities. The deformation mechanism, as predicted from stacking fault energies, agree well with experimental observations of deformed nanostructures that the dislocations are primarily observed in the Cu-rich phase. Based on the above results, we discuss and propose the alloy design strategy for controlling phase and deformation heterogeneities via the GB segregation engineering and the tuning of phase composition and fraction. It is recommended to investigate the effect of a quaternary element on GB segregation and heterogeneous phase transitions and conduct mechanical tests to validate the correlation between alloy composition and yield strength in future experimental studies. The study will help to guide the composition design for controlling the heterogeneous phase transition and for achieving better mechanical properties in noble-metal Au-Ag-Cu-based multicomponent alloys.

Author Contributions: Conceptualization, B.Z., H.G. and X.R.; methodology, B.Z., L.F. and H.G.; software, B.Z.; validation, L.F.; formal analysis, X.R.; investigation, B.Z., L.F., H.G., X.R., K.X. and J.H.; resources, Y.M.; data curation, B.Z.; writing—original draft preparation, B.Z.; writing—review and editing, X.R. and H.G.; visualization, B.Z.; supervision, Y.M.; project administration, Y.M.; funding acquisition, Y.M. All authors have read and agreed to the published version of the manuscript.

Funding: This work was funded by the Yunnan Science and Technology Projects (Grant. No. 202002AB080001-6, 202205AF150020, 202201AS070065).

Data Availability Statement: The data presented in this study are available on request from the corresponding author.

Acknowledgments: The authors acknowledge the computational support provided by the Advanced Computing Center of Yunnan University.

Conflicts of Interest: The authors declare no conflict of interest. The funders had no role in the design of the study; in the collection, analyses, or interpretation of data; in the writing of the manuscript; or in the decision to publish the results.

References

1. Tytko, D.; Choi, P.-P.; Klöwer, J.; Kostka, A.; Inden, G.; Raabe, D. Microstructural evolution of a Ni-based superalloy (617B) at 700 °C studied by electron microscopy and atom probe tomography. *Acta Mater.* **2012**, *60*, 1731–1740. [CrossRef]
2. Liu, L.; Yu, Q.; Wang, Z.; Ell, J.; Huang, M.X.; Ritchie, R.O. Making ultrastrong steel tough by grain-boundary delamination. *Science* **2020**, *368*, 1347–1352. [CrossRef]
3. Gong, M.M.; Dey, S.; Wu, L.J.; Chang, C.H.; Li, H.; Castro, R.H.R.; Liu, F. Effects of concurrent grain boundary and surface segregation on the final stage of sintering: The case of Lanthanum doped yttria-stabilized zirconia. *J. Mater. Sci. Technol.* **2017**, *33*, 251–260. [CrossRef]
4. Zhou, Y.-N.; Ma, Y.; Shi, Z.-N.; Zhou, J.-C.; Dong, B.; Li, M.-X.; Wang, F.-G.; Liu, B.; Yu, J.-F.; Chai, Y.-M. Boosting oxygen evolution by nickel nitrate hydroxide with abundant grain boundaries via segregated high-valence molybdenum. *J. Colloid Interface Sci.* **2022**, *613*, 224–233. [CrossRef] [PubMed]
5. Ming, K.; Li, L.; Li, Z.; Bi, X.; Wang, J. Grain boundary decohesion by nanoclustering Ni and Cr separately in CrMnFeCoNi high-entropy alloys. *Sci. Adv.* **2019**, *5*, eaay0639. [CrossRef] [PubMed]
6. Sathiyamoorthi, P.; Basu, J.; Kashyap, S.; Pradeep, K.G.; Kottada, R.S. Thermal stability and grain boundary strengthening in ultrafine-grained CoCrFeNi high entropy alloy composite. *Mater. Des.* **2017**, *134*, 426–433. [CrossRef]
7. Rajeshwari, K.S.; Sankaran, S.; Hari Kumar, K.C.; Rösner, H.; Peterlechner, M.; Esin, V.A.; Divinski, S.; Wilde, G. Grain boundary diffusion and grain boundary structures of a Ni-Cr-Fe- alloy: Evidences for grain boundary phase transitions. *Acta Mater.* **2020**, *195*, 501–518. [CrossRef]
8. Thapliyal, S.; Agrawal, P.; Agrawal, P.; Nene, S.S.; Mishra, R.S.; McWilliams, B.A.; Cho, K.C. Segregation engineering of grain boundaries of a metastable Fe-Mn-Co-Cr-Si high entropy alloy with laser-powder bed fusion additive manufacturing. *Acta Mater.* **2021**, *219*, 117271. [CrossRef]
9. Zhou, N.; Hu, T.; Luo, J. Grain boundary complexions in multicomponent alloys: Challenges and opportunities. *Curr. Opin. Solid State Mater. Sci.* **2016**, *20*, 268–277. [CrossRef]
10. Mayer, K.M.; Hafner, J.H. Localized Surface Plasmon Resonance Sensors. *Chem. Rev.* **2011**, *111*, 3828–3857. [CrossRef]
11. Udoh, K.I.; Fujiyama, H.; Hisatsune, K.; Hasaka, M.; Yasuda, K. Age-hardening associated with ordering and spinodal decomposition in a AgCu-40 at % Au pseudobinary alloy. *J. Mater. Sci.* **1992**, *27*, 504–510. [CrossRef]
12. Romig, A.D.; Dugger, M.T.; McWhorter, P.J. Materials issues in microelectromechanical devices: Science, engineering, manufacturability and reliability. *Acta Mater.* **2003**, *51*, 5837–5866. [CrossRef]
13. Yasuhara, A.; Sannomiya, T. Atomically localized ordered phase and segregation at grain boundaries in Au–Ag–Cu ternary alloy nanoparticles. *J. Phys. Chem. C* **2022**, *126*, 1160–1167. [CrossRef]
14. Yasuhara, A.; Kubo, K.; Yanagimoto, S.; Sannomiya, T. Thermodynamic Tuning of Au–Ag–Cu Nanoparticles with Phase Separation and Ordered Phase Formation. *J. Phys. Chem. C* **2020**, *124*, 15481–15488. [CrossRef]
15. Chatterjee, K.; Howe, J.M.; Johnson, W.C.; Murayama, M. Static and in situ TEM investigation of phase relationships, phase dissolution, and interface motion in Ag–Au–Cu alloy nanoparticles. *Acta Mater.* **2004**, *52*, 2923–2935. [CrossRef]
16. Prince, A. Critical assessment of copper–gold–silver ternary system. *Int. Mater. Rev.* **1988**, *33*, 314–338. [CrossRef]
17. Ntukogu, T.O.; Cadoff, I.B. Tie line compositions of ternary Cu–Ag–Au alloys within miscibility gap. *Mater. Sci. Technol.* **1986**, *2*, 528–533. [CrossRef]
18. Kusoffsky, A. Thermodynamic evaluation of the ternary Ag–Au–Cu system—Including a short range order description. *Acta Mater.* **2002**, *50*, 5139–5145. [CrossRef]
19. Kim, H.I.; Lee, D.H.; Sim, J.S.; Kwon, Y.H.; Seol, H.J. Age-hardening by miscibility limit of Au-Pt and Ag-Cu systems in an Au-Ag-Cu-Pt alloy. *Mater. Charact.* **2009**, *60*, 357–362. [CrossRef]
20. Amiour, L.; Hamana, D.; Chetibi, L. Microstructural evolution of Au–35 mass% Ag–15 mass% Cu alloy during ageing at 415 °C. *J. Therm. Anal. Calorim.* **2020**, *146*, 2343–2351. [CrossRef]
21. Nakagawa, M.; Yasuda, K. Age-hardening and the associated phase transformation in an Au-55.2 at% Cu-17.4 at% Ag ternary alloy. *J. Mater. Sci.* **1988**, *23*, 2975–2982. [CrossRef]
22. Seol, H.-J.; Kim, G.-C.; Son, K.-H.; Kwon, Y.H.; Kim, H.-I. Hardening mechanism of an Ag–Pd–Cu–Au dental casting alloy. *J. Alloys Compd.* **2005**, *387*, 139–146. [CrossRef]
23. Hisatsune, K.; Udoh, K.-I.; Sosrosoedirdjo, B.I.; Tani, T.; Yasuda, K. Age-hardening characteristics in an AuCu-14at.%Ag alloy. *J. Alloys Compd.* **1991**, *176*, 269–283. [CrossRef]

24. Lee, S.H.; Lim, I.S.; Cho, M.H.; Pyo, A.R.; Kwon, Y.H.; Seol, H.J.; Kim, H.I. Age-hardening and overaging mechanisms related to the metastable phase formation by the decomposition of Ag and Cu in a dental Au-Ag-Cu-Pd-Zn alloy. *Gold Bull.* **2011**, *44*, 155–162. [CrossRef]
25. Ding, Q.; Zhang, Y.; Chen, X.; Fu, X.; Chen, D.; Chen, S.; Gu, L.; Wei, F.; Bei, H.; Gao, Y.; et al. Tuning element distribution, structure and properties by composition in high-entropy alloys. *Nature* **2019**, *574*, 223–227. [CrossRef]
26. Meiners, T.; Frolov, T.; Rudd, R.E.; Dehm, G.; Liebscher, C.H. Observations of grain-boundary phase transformations in an elemental metal. *Nature* **2020**, *579*, 375–378. [CrossRef]
27. Yin, S.; Ding, J.; Asta, M.; Ritchie, R.O. Ab initio modeling of the energy landscape for screw dislocations in body-centered cubic high-entropy alloys. *NPJ Comput. Mater.* **2020**, *6*, 110. [CrossRef]
28. Varvenne, C.; Curtin, W.A. Predicting yield strengths of noble metal high entropy alloys. *Scr. Mater.* **2018**, *142*, 92–95. [CrossRef]
29. Li, H.; Zong, H.; Li, S.; Jin, S.; Chen, Y.; Cabral, M.J.; Chen, B.; Huang, Q.; Chen, Y.; Ren, Y.; et al. Uniting tensile ductility with ultrahigh strength via composition undulation. *Nature* **2022**, *604*, 273–279. [CrossRef]
30. van de Walle, A. Multicomponent multisublattice alloys, nonconfigurational entropy and other additions to the Alloy Theoretic Automated Toolkit. *Calphad* **2009**, *33*, 266–278. [CrossRef]
31. Zhou, X.; Tehranchi, A.; Curtin, W.A. Mechanism and Prediction of Hydrogen Embrittlement in fcc Stainless Steels and High Entropy Alloys. *Phys. Rev. Lett.* **2021**, *127*, 175501. [CrossRef] [PubMed]
32. Zhou, X.; Curtin, W.A. First principles study of the effect of hydrogen in austenitic stainless steels and high entropy alloys. *Acta Mater.* **2020**, *200*, 932–942. [CrossRef]
33. Kresse, G.; Furthmuller, J. Efficient iterative schemes for ab initio total-energy calculations using a plane-wave basis set. *Phys. Rev. B* **1996**, *54*, 11169–11186. [CrossRef]
34. Blöchl, P.E. Projector augmented-wave method. *Phys. Rev. B* **1994**, *50*, 17953–17979. [CrossRef] [PubMed]
35. Kresse, G.; Joubert, D. From ultrasoft pseudopotentials to the projector augmented-wave method. *Phys. Rev. B* **1999**, *59*, 1758–1775. [CrossRef]
36. Perdew, J.P.; Chevary, J.A.; Vosko, S.H.; Jackson, K.A.; Pederson, M.R.; Singh, D.J.; Fiolhais, C. Atoms, molecules, solids, and surfaces: Applications of the generalized gradient approximation for exchange and correlation. *Phys. Rev. B* **1992**, *46*, 6671–6687. [CrossRef]
37. Perdew, J.P.; Burke, K.; Ernzerhof, M. Generalized gradient approximation made simple. *Phys. Rev. Lett.* **1996**, *77*, 3865–3868. [CrossRef]
38. Scheiber, D. Segregation and embrittlement of gold grain boundaries. *Comput. Mater. Sci.* **2021**, *187*, 110110. [CrossRef]
39. Haas, P.; Tran, F.; Blaha, P. Calculation of the lattice constant of solids with semilocal functionals. *Phys. Rev. B* **2009**, *79*, 085104. [CrossRef]
40. Methfessel, M.; Paxton, A.T. High-precision sampling for Brillouin-zone integration in metals. *Phys. Rev. B* **1989**, *40*, 3616–3621. [CrossRef]
41. Monkhorst, H.J.; Pack, J.D. Special points for Brillouin-zone integrations. *Phys. Rev. B* **1976**, *13*, 5188–5192. [CrossRef]
42. Findik, F. Improvements in spinodal alloys from past to present. *Mater. Des.* **2012**, *42*, 131–146. [CrossRef]
43. George, E.P.; Curtin, W.A.; Tasan, C.C. High entropy alloys: A focused review of mechanical properties and deformation mechanisms. *Acta Mater.* **2020**, *188*, 435–474. [CrossRef]
44. Lee, C.; Song, G.; Gao, M.C.; Feng, R.; Chen, P.; Brechtl, J.; Chen, Y.; An, K.; Guo, W.; Poplawsky, J.D.; et al. Lattice distortion in a strong and ductile refractory high-entropy alloy. *Acta Mater.* **2018**, *160*, 158–172. [CrossRef]
45. Zheng, H.; Li, X.-G.; Tran, R.; Chen, C.; Horton, M.; Winston, D.; Persson, K.A.; Ong, S.P. Grain boundary properties of elemental metals. *Acta Mater.* **2020**, *186*, 40–49. [CrossRef]
46. Born, M.; Huang, K. Dynamical Theory of Crystal Lattices. *Am. J. Phys.* **1955**, *23*, 474. [CrossRef]
47. Chen, X.; Niu, H.; Li, D.; Li, Y. Modeling hardness of polycrystalline materials and bulk metallic glasses. *Intermetallics* **2011**, *19*, 1275–1281. [CrossRef]
48. Zhai, W.; Bai, L.; Zhou, R.; Fan, X.; Kang, G.; Liu, Y.; Zhou, K. Recent Progress on Wear-Resistant Materials: Designs, Properties, and Applications. *Adv. Sci.* **2021**, *8*, 2003739. [CrossRef]
49. Leyland, A.; Matthews, A. On the significance of the H/E ratio in wear control: A nanocomposite coating approach to optimised tribological behaviour. *Wear* **2000**, *246*, 1–11. [CrossRef]
50. Pei, Z.; Dutta, B.; Kormann, F.; Chen, M. Hidden Effects of Negative Stacking Fault Energies in Complex Concentrated Alloys. *Phys. Rev. Lett.* **2021**, *126*, 255502. [CrossRef]
51. Shih, M.; Miao, J.; Mills, M.; Ghazisaeidi, M. Stacking fault energy in concentrated alloys. *Nat. Commun.* **2021**, *12*, 3590. [CrossRef] [PubMed]
52. Jin, Z.H.; Dunham, S.T.; Gleiter, H.; Hahn, H.; Gumbsch, P. A universal scaling of planar fault energy barriers in face-centered cubic metals. *Scr. Mater.* **2011**, *64*, 605–608. [CrossRef]
53. Rice, J.R. Dislocation nucleation from a crack tip: An analysis based on the Peierls concept. *J. Mech. Phys. Solids* **1992**, *40*, 239–271. [CrossRef]
54. Mayahi, R. An investigation concerning generalized stacking fault behavior of AlCoxCrFeNi ($0.25 \leq x \leq 2$) high entropy alloys: Insights from first-principles study. *J. Alloys Compd.* **2020**, *818*, 152928. [CrossRef]

55. Li, L.; Li, Z.; Kwiatkowski da Silva, A.; Peng, Z.; Zhao, H.; Gault, B.; Raabe, D. Segregation-driven grain boundary spinodal decomposition as a pathway for phase nucleation in a high-entropy alloy. *Acta Mater.* **2019**, *178*, 1–9. [CrossRef]
56. Kwiatkowski da Silva, A.; Kamachali, R.D.; Ponge, D.; Gault, B.; Neugebauer, J.; Raabe, D. Thermodynamics of grain boundary segregation, interfacial spinodal and their relevance for nucleation during solid-solid phase transitions. *Acta Mater.* **2019**, *168*, 109–120. [CrossRef]
57. Kwiatkowski da Silva, A.; Ponge, D.; Peng, Z.; Inden, G.; Lu, Y.; Breen, A.; Gault, B.; Raabe, D. Phase nucleation through confined spinodal fluctuations at crystal defects evidenced in Fe-Mn alloys. *Nat. Commun.* **2018**, *9*, 1137. [CrossRef]
58. Sun, F.; Miyamoto, G.; Liu, Y.; Hayasaka, Y.; Furuhara, T. Phase separation with ordering in aged Fe-Ni-Mn medium entropy alloy. *Acta Mater.* **2021**, *223*, 117487. [CrossRef]
59. Thiel, F.; Geissler, D.; Nielsch, K.; Kauffmann, A.; Seils, S.; Heilmaier, M.; Utt, D.; Albe, K.; Motylenko, M.; Rafaja, D.; et al. Origins of strength and plasticity in the precious metal based high-entropy alloy AuCuNiPdPt. *Acta Mater.* **2020**, *185*, 400–411. [CrossRef]
60. Robson, J.D. Modeling competitive continuous and discontinuous precipitation. *Acta Mater.* **2013**, *61*, 7781–7790. [CrossRef]
61. Xing, W.; Kalidindi, A.R.; Amram, D.; Schuh, C.A. Solute interaction effects on grain boundary segregation in ternary alloys. *Acta Mater.* **2018**, *161*, 285–294. [CrossRef]
62. Hu, C.; Luo, J. Data-driven prediction of grain boundary segregation and disordering in high-entropy alloys in a 5D space. *Mater. Horiz.* **2022**, *9*, 1023–1035. [CrossRef] [PubMed]
63. Murdoch, H.A.; Schuh, C.A. Estimation of grain boundary segregation enthalpy and its role in stable nanocrystalline alloy design. *J. Mater. Res.* **2013**, *28*, 2154–2163. [CrossRef]
64. Darvishi Kamachali, R.; Kwiatkowski da Silva, A.; McEniry, E.; Ponge, D.; Gault, B.; Neugebauer, J.; Raabe, D. Segregation-assisted spinodal and transient spinodal phase separation at grain boundaries. *NPJ Comput. Mater.* **2020**, *6*, 191. [CrossRef]
65. Fan, L.; Yang, T.; Luan, J.H.; Jiao, Z.B. Control of discontinuous and continuous precipitation of γ'-strengthened high-entropy alloys through nanoscale Nb segregation and partitioning. *J. Alloys Compd.* **2020**, *832*, 154903. [CrossRef]
66. Suhane, A.; Scheiber, D.; Popov, M.; Razumovskiy, V.I.; Romaner, L.; Militzer, M. Solute drag assessment of grain boundary migration in Au. *Acta Mater.* **2022**, *224*, 117473. [CrossRef]
67. Zhang, J.; Ma, S.; Xiong, Y.; Xu, B.; Zhao, S. Elemental partitions and deformation mechanisms of L12-type multicomponent intermetallics. *Acta Mater.* **2021**, *219*, 117238. [CrossRef]
68. Ding, J.; Yu, Q.; Asta, M.; Ritchie, R.O. Tunable stacking fault energies by tailoring local chemical order in CrCoNi medium-entropy alloys. *Proc. Natl. Acad. Sci. USA* **2018**, *115*, 8919–8924. [CrossRef]
69. Yin, B.; Curtin, W.A. First-principles-based prediction of yield strength in the RhIrPdPtNiCu high-entropy alloy. *NPJ Comput. Mater.* **2019**, *5*, 14. [CrossRef]